



## Surpassing Pt hydrogen production from {200} facet-riched polyhedral Rh<sub>2</sub>P nanoparticles by one-step synthesis

Hongqiang Xin<sup>a</sup>, Lan Sun<sup>a</sup>, Yiwei Zhao<sup>a</sup>, Zhengfei Dai<sup>a</sup>, Qiaomei Luo<sup>a</sup>, Shengwu Guo<sup>a</sup>, Danyang Li<sup>a</sup>, Ya Chen<sup>a</sup>, Naoki Ogiwara<sup>c</sup>, Hiroshi Kitagawa<sup>c</sup>, Bo Huang<sup>b,\*</sup>, Fei Ma<sup>a,\*</sup>

<sup>a</sup> State Key Laboratory for Mechanical Behaviour of Materials, Xi'an Jiaotong University, Beilin Ward, Xi'an 710049, China

<sup>b</sup> School of Chemical Engineering and Technology, Xi'an Jiaotong University, Beilin Ward, Xi'an 710049, China

<sup>c</sup> Division of Chemistry, Graduate School of Science, Kyoto University, Kitashirakawa-Oiwakecho, Sakyo-ku, Kyoto 606-8502, Japan



### ARTICLE INFO

#### Keywords:

Rhodium phosphide  
Hydrogen evolution reaction  
Morphology control  
Active facet  
Density functional theory calculation

### ABSTRACT

The efficient water electrolysis catalyst is prominently important and urgent to forward the widespread applications of hydrogen energy. In this work, polyhedral-morphology controlled rhodium phosphide (Rh<sub>2</sub>P) nanoparticles are synthesized by one-step high temperature pyrolysis under Ar atmosphere at 90 Pa. By analyzing the morphologies of Rh<sub>2</sub>P, the crystal facets of {200}, {220} and {111} are dominant in the 26-facet polyhedrons, and {200} facets account for 58% of the total surface area of polyhedral 26-facet shapes. The overpotentials of polyhedral Rh<sub>2</sub>P NPs are 12.6 mV and 10.5 mV at 10 mA m<sup>-2</sup> in 0.5 M H<sub>2</sub>SO<sub>4</sub> and 1 M KOH electrolytes, even lower than those of Pt/C. Theoretical calculations indicate that {200} facets of Rh<sub>2</sub>P NPs have the highest catalytic activity among {200}, {111}, and {220}, with the lowest hydrogen adsorption free energy. The substantial exposure of {200} facets is beneficial to the high catalytic activity of Rh<sub>2</sub>P NPs.

### 1. Introduction

Hydrogen energy has been deemed as an ideal energy source with more efficient and green power, which is promising to solve the emergence of the energy crisis and environmental pollution from the traditional fossil fuels [1–3]. Electrochemical water splitting has been regarded as an efficient and eco-friendly pathway for producing high-purity hydrogen in comparison with the existing hydrogen production technologies [4–7]. Hydrogen evolution reaction (HER) as important reaction in water splitting, and the key HER catalysts have been widely exploited [8–11]. Based on the Sabatier's principle, ideal catalysts usually possess near-neutral Gibbs free energy of hydrogen adsorption ( $\Delta G_{\text{H}^*} \approx 0$ ) for accelerating the sluggish kinetics of the HER [12–15].

Transition metal phosphides (TMPs) have been widely considered as a hopeful substitute for the benchmark Pt/C catalyst, such as rhodium phosphide (Rh<sub>2</sub>P) [16–18]. The high catalytic activities of TMPs may stem from the modulated electronic structures of metal atoms by the outermost phosphorus, which facilitates the favorable  $\Delta G_{\text{H}^*}$  for HER process [19,20]. Well-defined surface structures of catalysts are also beneficial to boost HER performance [21–24], and the catalytic

activities are commonly enhanced through morphology-controlled syntheses. For example, monodisperse Rh<sub>2</sub>P nanoparticles, ultrathin Rh<sub>2</sub>P nanosheets, dendritic PtRh alloyed, and 3D Rh/Rh<sub>2</sub>P nano-flake assemblies have been reported as the outstanding HER catalysts [25–29]. Although surface morphology and the exposed facets of Rh<sub>2</sub>P are believed to greatly affect the HER catalytic activity, the constitutive relation between the HER activity and the exposed crystal planes of polyhedral Rh<sub>2</sub>P is still not understood. Moreover, owing to the extraordinarily high surface energy of metallic Rh, morphology-controlled Rh<sub>2</sub>P was mainly synthesized with a two-step seed-mediated growth method [30,31]. It is still challenging to synthesize Rh<sub>2</sub>P with controlled morphologies and exposed facets by a one-step reaction method.

In this study, polyhedral Rh<sub>2</sub>P NPs were synthesized by one-step pyrolysis of Rh metalorganic compound at high temperature under low-pressure inert condition. The morphology evolution of Rh<sub>2</sub>P was investigated in the reaction temperature ranging from 500° to 1000°C, and it was found that the morphology and sizes of Rh<sub>2</sub>P NPs were strongly affected by the reaction temperature. In particular, the Rh<sub>2</sub>P NPs synthesized at 900 °C (Rh<sub>2</sub>P-900) exhibited polyhedral shapes. The polyhedral Rh<sub>2</sub>P-900 NPs have the lowest overpotentials of 12.6 and

\* Corresponding authors.

E-mail addresses: [bohuang@xjtu.edu.cn](mailto:bohuang@xjtu.edu.cn) (B. Huang), [mafei@mail.xjtu.edu.cn](mailto:mafei@mail.xjtu.edu.cn) (F. Ma).

10.5 mV at 10 mA cm<sup>-2</sup> in acidic and alkaline media, respectively, even remarkably better than those of commercial Pt/C (26.8 and 40.2 mV). The experimental characterizations on the exposed facets and the theoretical calculations were performed to analyze and understand the enhanced catalytic activity.

## 2. Experimental section

### 2.1. Chemicals

Bis(triphenylphosphine)rhodium(I) carbonyl chloride [Rh(CO)Cl (PPh<sub>3</sub>)<sub>2</sub>, 99%] and Rhodium(II) acetate dimer [Rh<sub>2</sub>(OAc)<sub>4</sub>, 99.99% trace metals basis] were purchased from TCI Co., Ltd. Tris(triphenylphosphine)rhodium(I) chloride [Rh(PPh<sub>3</sub>)<sub>3</sub>Cl, 98%] and Potassium Hexachlororhodate(III) [K<sub>3</sub>RhCl<sub>6</sub>, 98%], and Potassium hydroxide (KOH, 99.99%) were acquired from Adamas Reagent, Ltd. Carbon black, Commercial Pt/C (20%) catalyst, Sodium borohydride (NaBH<sub>4</sub>, 98%) and Nafion D-521 (5%) were purchased from Alfa Aesar. Sulfuric acid (H<sub>2</sub>SO<sub>4</sub>, 98%) was acquired from Sinopharm Chemical Reagent Co., Ltd. All chemical reagents were adopted in this experiment without further purification.

### 2.2. Synthesis of Rh/C NPs, Rh/Rh<sub>2</sub>P, and Rh<sub>2</sub>P NPs

Rh/C NPs were synthesized by wet chemical reaction. Firstly, K<sub>3</sub>RhCl<sub>6</sub> (10 mg, 0.023 mmol), 5 mg carbon black and 10 ml deionized water were dissolved and stirred to gain a homogeneous aqueous solution A. Secondly, NaBH<sub>4</sub> (13 mg, 0.3465 mmol) was put into 2 ml deionized water to form solution B. Then, solutions A and B were mixed. At last, the mixture was centrifuged, washed, and dried to produce the black powder of Rh/C NPs. Rh/Rh<sub>2</sub>P NPs were synthesized from pyrolytic Rh precursor [Rh(PPh<sub>3</sub>)<sub>3</sub>Cl] (50 mg, 0.054 mmol) in a tube CVD furnace under reductive conditions (H<sub>2</sub> (5%)/Ar) with the flow rate of 100 sccm at 600 °C and under 90 Pa for 2 h, and then cooled down to room temperature. The reaction products were black powders. Rh<sub>2</sub>P NPs black powders were obtained under 90 Pa Ar atmosphere at 500, 600, 700, 800, 900 and 1000 °C for 2 h. The other preparation procedures were the same as described above. In the high temperature and inert ambient, carbon could also be formed due to the pyrolytic carbonization of organic ligands.

### 2.3. Microstructural characterizations

The phases were analyzed by powder X-ray diffraction (Bruker D8 Advance diffractometer with Cu-K<sub>α</sub> radiation,  $\lambda = 1.5406 \text{ \AA}$ ). The morphologies were measured by field-emission scanning electron microscopy (JSM-7000 F), TEM (JEOL JEM 2100 F) and HAADF-STEM (JEOL JEM-F200). X-ray photoelectron spectroscopy (XPS) was detected by the Thermo Scientific KAlpha XPS instrument. The XANES and EXAFS of the Rh K-edge ( $E_0 = 23,220 \text{ eV}$ ) were characterized on the BL14B2 beamline, Spring-8. Rh(CO)Cl(PPh<sub>3</sub>)<sub>2</sub> and Rh<sub>2</sub>(OAc)<sub>4</sub> were selected as references, named Rh(I) and Rh(II), respectively. For wavelet transform analysis, the  $\chi(k)$  exported from Athena was imported into the Hama Fortran code. The parameters were listed as follows: R range, 1–4 Å, k range, 0–11 Å<sup>-1</sup>; k weight, 3; and Morlet function with  $\kappa = 10$ ,  $\sigma = 1$  was used as the mother wavelet to provide the overall distribution.

### 2.4. Method in morphology

It was indeed difficult to accurately determine the shapes of Rh<sub>2</sub>P NPs from the HRTEM images because of its projection observation. In the 200 kV JEOL 2100 F electron microscope, the sample can be tilted in the range from -20 to + 20°. For a given sample, more than 150 nanoparticles had been characterized, which could provide reasonable results. The interplanar distance and the angles between crystallographic planes can easily be measured from the HRTEM images as well

as from the fast Fourier transformation (FFT). Moreover, a slight tilt of the nanoparticles might induce drastic changes of the image contrast, so the simulation of the HRTEM image was also required for the exact resolution of the nanoparticles, which was phase contrast formed by the interference of the diffracted beams and the direct incidence beam. The diffractogram from FFT was used to reveal the orientation relationship. Moreover, the inverse FFT for the selected spots could be used to obtain a virtual HRTEM image. Morphology-controlled syntheses of Rh<sub>2</sub>P polyhedrons were composed of 26-facet polyhedrons of rhombicuboctahedron, bevelled cube, and great rhombicuboctahedron containing 6 {100}, 12 {110}, and 8 {111} planes, and these models were simulated by the VEST soft.

### 2.5. Electrochemical measurements

The obtained homogeneous catalyst ink (10 µl) was deposited on the glassy carbon (3 mm diameter) working electrode. The preparation of catalyst ink and an electrode deposited catalyst ink were prepared according to the normal procedure [32]. A standard three-electrode configuration was implemented in the electrochemical measurements by the electrochemical workstation (Autolab PGSTAT 128 N) with graphite rod (6 mm) counter electrode and Ag/AgCl (3.5 M KCl) reference electrode. Linear sweep voltammetry curves (LSV) were measured in a scan rate of 5 mV s<sup>-1</sup>. The electrolyte for HER is the N<sub>2</sub> saturated KOH (1.0 M) or H<sub>2</sub>SO<sub>4</sub> (0.5 M) electrolytes. The Nyquist plots of electrochemical impedance spectroscopy (EIS) were tested in the frequency range from 100 kHz to 1 Hz with an alternating current amplitude of 10 mV. For the electrochemical active surface area (ECSA) test, the electric double layer capacitance ( $C_{dl}$ ) was evaluated by cyclic voltammetry (CV) with the scanning rates of 20, 40, 60, 80, 100 and 120 mV s<sup>-1</sup>.

### 2.6. Computational methods and models

The theoretical calculations were implemented by Vienna Ab-initio Simulation Package (VASP), based on the plane-wave pseudopotential technique [33]. The generalized gradient approximation (GGA) by Perdew–Burke–Ernzerhof (PBE) was carried out to describe the exchange-correlation function [34]. A suitable cut-off energy (400 eV) and energy convergence criterion ( $10^{-6}$  eV) were set. And all the structures were relaxed using the conjugate gradient method until the force was smaller than 0.01 eV/Å. To eliminate the interaction between adjacent images caused by periodicity, a 15 Å vacuum layer was added in the z-axis direction of all models. During the structural relaxation, the two bottom layers were fixed, while all the other atoms were fully relaxed. The Monkhorst–Pack special k-point meshes were utilized to carry out Brillouin zone sampling [35]. In order to ensure that different crystal planes have the same number of active sites coverage,  $2 \times 2 \times 1$  k-point grids were used for  $6 \times 6 \times 4$  Rh<sub>2</sub>P (200),  $6 \times 4 \times 4$  Rh<sub>2</sub>P (220),  $6 \times 6 \times 4$  Rh<sub>2</sub>P (111) supercells,  $3 \times 3 \times 4$  Rh (111), and Pt (111) supercells, respectively, for both free-standing and adsorbed systems. The Gibbs free energy of hydrogen adsorption was calculated as  $\Delta G_{\text{H}^*} = \Delta E_{\text{H}^*} + \Delta E_{\text{ZPE}} - T\Delta S_{\text{H}^*}$ , in which  $\Delta E_{\text{H}^*}$ ,  $\Delta E_{\text{ZPE}}$ , and  $\Delta S_{\text{H}^*}$  represented the binding energy, zero point energy change, the change in zero energy, and entropy change of H<sup>\*</sup> adsorption, respectively [36]. Charge density difference study and Bader charge analysis were used to describe the electron transfer of the system.

## 3. Results and discussion

### 3.1. Phases and structures of Rh/C, Rh/Rh<sub>2</sub>P, and Rh<sub>2</sub>P catalysts

**Fig. 1a** schematically shows the synthetic route of Rh<sub>2</sub>P catalysts. The Rh<sub>2</sub>P catalysts were prepared by decomposing Rh(PPh<sub>3</sub>)<sub>3</sub>Cl under 90 Pa Ar atmosphere at 500, 600, 700, 800, 900, and 1000 °C for 2 h, which were denoted as Rh<sub>2</sub>P-500, Rh<sub>2</sub>P-600, Rh<sub>2</sub>P-700, Rh<sub>2</sub>P-800, Rh<sub>2</sub>P-900, and Rh<sub>2</sub>P-1000. **Fig. 1b** shows the XRD patterns of Rh/C, Rh/

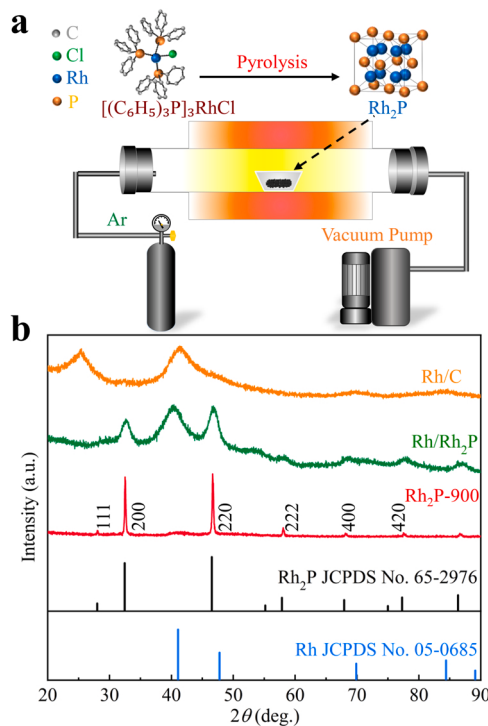


**Fig. 1.** The scheme for the preparation of Rh<sub>2</sub>P NPs and the structure characterization of products with PXRD measurements. (a) Schematic image of the preparation of Rh/Rh<sub>2</sub>P and Rh<sub>2</sub>P-900 by thermal decomposition of Rh precursor. (b) PXRD patterns of Rh/C (orange line), Rh/Rh<sub>2</sub>P (green line), and Rh<sub>2</sub>P-900 catalysts (red line).

Rh<sub>2</sub>P, and Rh<sub>2</sub>P-900 catalysts. For the Rh/C catalyst (orange line), a broad diffraction peak at 40.7° is associated with the metallic Rh (JCPDS No. 05-0685), and the other peak at 25.2° is assigned to the amorphous carbon. The peaks at 27.9°, 32.3°, 46.5°, 57.8°, 67.9°, and 77.5° in Rh<sub>2</sub>P-900 (red line) are indexed to the {111}, {200}, {220}, {222}, {400}, and

{420} planes of Rh<sub>2</sub>P (Fm-3 m) (JCPDS No. 65-2976). Fig. S1 displays the XRD patterns of Rh<sub>2</sub>P-500, Rh<sub>2</sub>P-600, Rh<sub>2</sub>P-700, Rh<sub>2</sub>P-800, Rh<sub>2</sub>P-900, and Rh<sub>2</sub>P-1000 to further understand the structural information of various Rh<sub>2</sub>P NPs. The XRD peaks of Rh<sub>2</sub>P samples become sharper with reaction temperature increasing from 500° to 1000°C, suggesting the enhanced crystallization. As well, the distinct diffraction peaks of Rh and Rh<sub>2</sub>P are detected in the Rh/Rh<sub>2</sub>P catalyst (green line).

The scanning electron microscope (SEM) and transmission electron microscope (TEM) images of Rh<sub>2</sub>P catalysts are displayed in the Fig. S2 and S3. The average sizes of Rh<sub>2</sub>P-500, Rh<sub>2</sub>P-600, Rh<sub>2</sub>P-700, Rh<sub>2</sub>P-800, Rh<sub>2</sub>P-900, and Rh<sub>2</sub>P-1000 NPs are  $3.0 \pm 0.6$  nm,  $5.8 \pm 1.8$  nm,  $10.2 \pm 3.2$  nm,  $14.4 \pm 7.6$  nm,  $17.3 \pm 5.1$  nm, and  $32.7 \pm 16.2$  nm (Fig. S3). As the reaction temperature is elevated, the size of Rh<sub>2</sub>P nanoparticles (NPs) becomes larger and larger gradually. Rh<sub>2</sub>P-900 NPs show more regular polyhedral morphology. However, if the temperature is further increased up to 1000 °C, Rh<sub>2</sub>P NPs grow into spherical shapes (Fig. S4–S9). That is, the morphology and sizes of Rh<sub>2</sub>P NPs are strongly affected by the reaction temperature. Figs. 2a and 2b show the SEM and TEM images of polyhedral Rh<sub>2</sub>P-900 NPs. The selected area electron diffraction (SAED) image (Fig. 2c) displays bright diffraction spots and rings, corresponding to the {200}, {220}, and {111} planes of Rh<sub>2</sub>P. The clear lattice fringes of HR-TEM image in Fig. 2d are ascribed to the {200}, {220}, and {111} planes of Rh<sub>2</sub>P. The magnified domain of the HR-TEM image (Fig. 2e) indicates that the distances of {200}, {220}, and {111} planes are 2.75, 1.94 and 3.12 Å, respectively. The angles between (200) and (111) planes, (022) and (111) planes are 54.7° and 35.3°. In addition, the TEM images, SAED images, and HR-TEM images of Rh/C and Rh/Rh<sub>2</sub>P catalysts are shown in Fig. S10 and S11. The energy-dispersive X-ray (EDX) maps (Fig. 2f–h) demonstrate the homogeneous distribution of Rh and P in the Rh<sub>2</sub>P-900. From the EDX spectra of Rh<sub>2</sub>P-900 (Fig. S12 and S13), the atomic ratio of the Rh and P in Rh<sub>2</sub>P-900 is 1: 0.5, which is consistent with the stoichiometric value [37].

In order to observe the morphological characteristics of Rh<sub>2</sub>P-900 polyhedron, a set of HRTEM images are displayed in Fig. 3. Fast Fourier transform (FFT) and inverse FFT (IFFT) are adopted to improve the contrast [38]. The HRTEM images (Fig. 3a–d), the FFT patterns

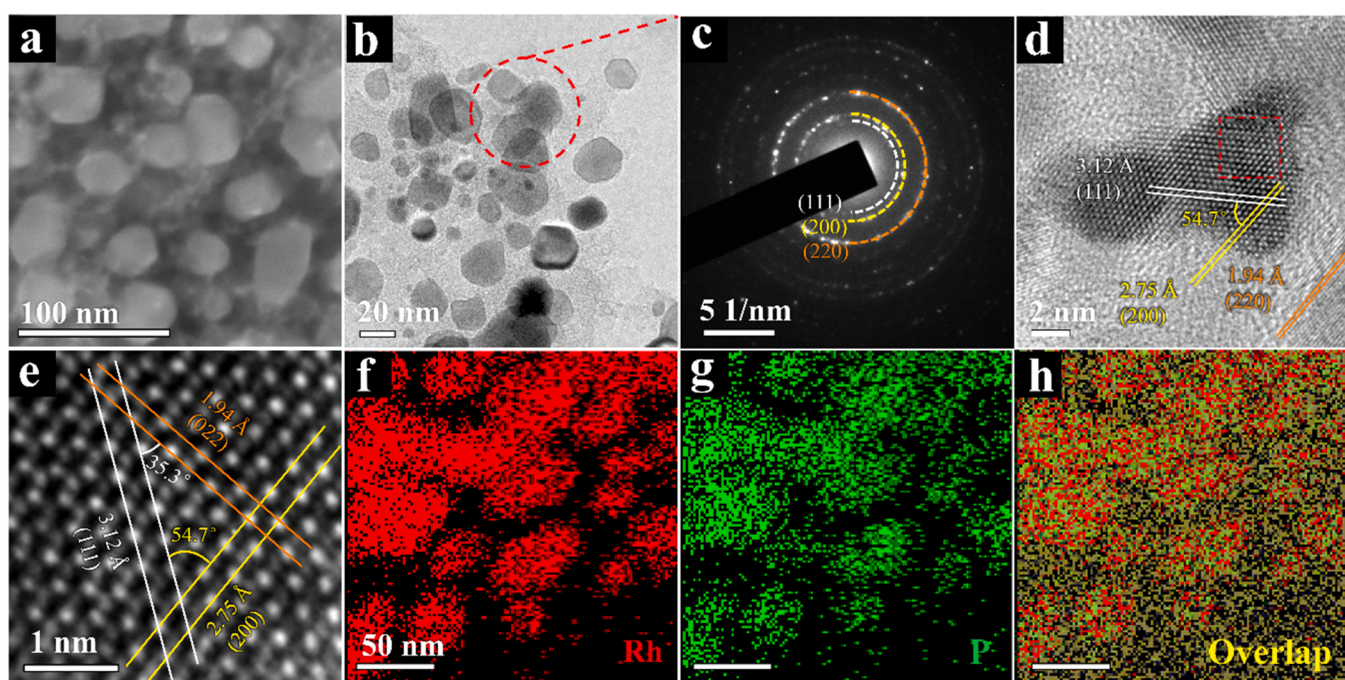


**Fig. 2.** The morphology of Rh<sub>2</sub>P. (a) SEM image, (b) bright field TEM image, (c) SAED pattern, (d) HR-TEM image, (e) Magnified domains with the red dashed square in (d), (f-h) HAADF-STEM element mapping.

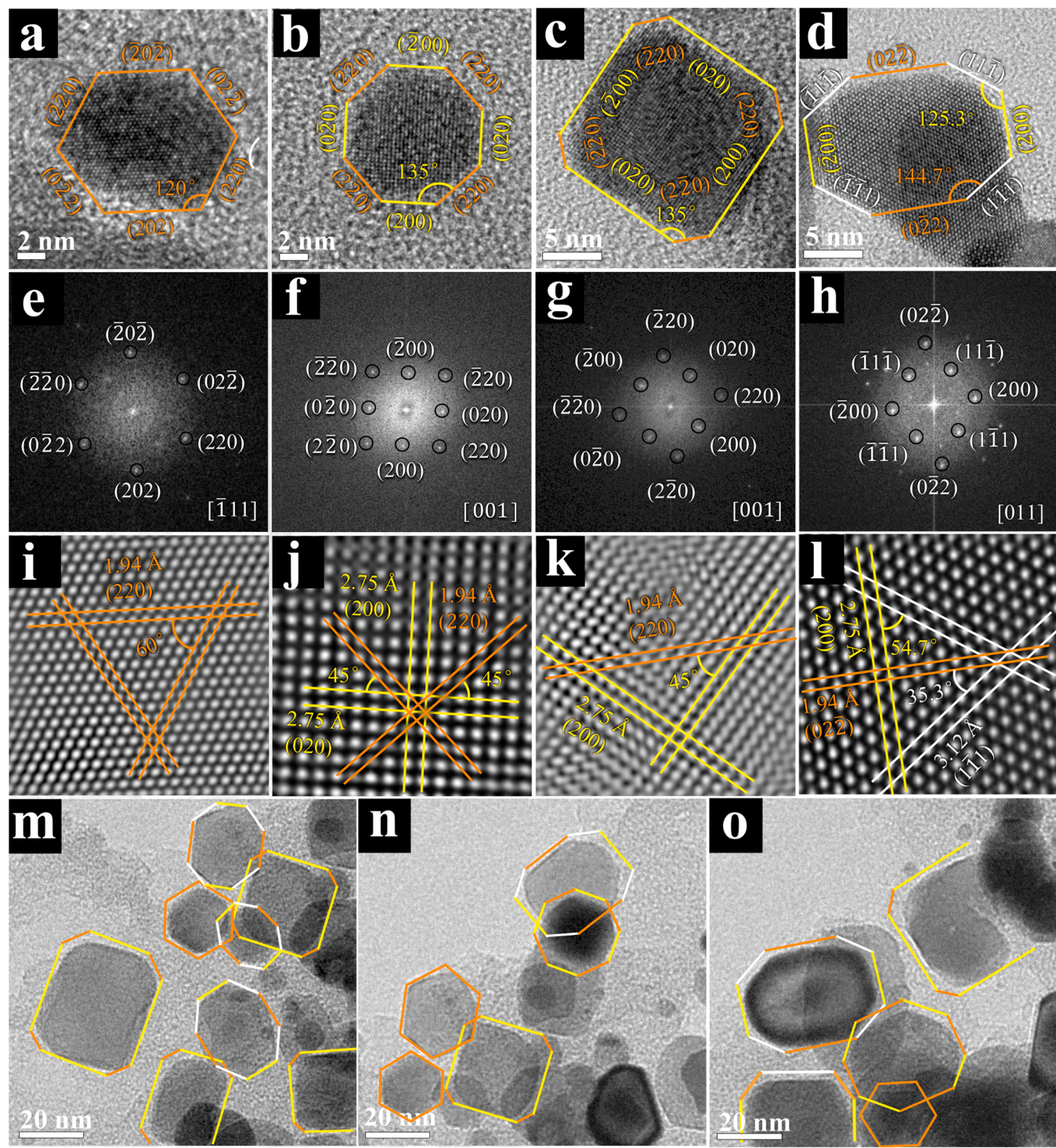


**Fig. 3.** The different projected shapes of Rh<sub>2</sub>P-900 NPs. (a–d) HRTEM images concerning different projected shapes of hexagonal-a (H-a), octagonal-b (O-b), octagonal-c (O-c), and octagonal-d (O-d). (e–h) Fast Fourier transform (FFT) diffractograms, corresponding to the column images in Fig. 3a–d, (i–l) Inverse fast Fourier transform (IFFT) images corresponds to the Fig. 3e–h. (m–o) TEM images of Rh<sub>2</sub>P-900 NPs.

(Fig. 3e–h) and the IFFT images (Fig. 3i–l) of Rh<sub>2</sub>P-900 NPs exhibit high contrast and high resolution. As displayed in Fig. 3a–d, Rh<sub>2</sub>P-900 NPs are polygonal, and according to the shapes, they are denoted as hexagonal-a (H-a) of Fig. 3a, octagonal-b (O-b) of Fig. 3b, octagonal-c (O-c) of Fig. 3c and octagonal-d (O-d) of Fig. 3d. More HRTEM images of Rh<sub>2</sub>P-900 NPs with regular polygons are shown in Fig. S14. Rh<sub>2</sub>P is identified according to the angles and distances between the atomic planes in IFFT (Fig. 3i–l). The projected outlines of a given Rh<sub>2</sub>P-900

particle can be drawn, referencing the FFT images. For example, {200}, {220}, and {111} facets are included in the octagonal shape (Fig. 3d), which is further proved by the FFT pattern and the IFFT image in Fig. 3h and Fig. 3l, respectively. The same processes have also been implemented for the other projection outlines in Fig. 3a–c.

According to the HRTEM images in Fig. S15a–d, the typically projected outlines and morphological models of Rh<sub>2</sub>P-900 NPs are shown in Fig. S15e–h. Although the projected shapes in Fig. S16a and Fig. S16b

are different, they have indeed projected along [111] and [001] orientations from the same 26-facet polyhedrons (Fig. S15a–d). The projected shapes of Rh<sub>2</sub>P-900 include the ideal 26-facet polyhedrons containing rhombicuboctahedron (Fig. S15i–j, m–n), bevelled cube (Fig. S15k, o) and great rhombicuboctahedron (Fig. S15l, p). All the Rh<sub>2</sub>P-900 nanocrystals are mainly enclosed by the {200}, {220}, and {111} facets. As listed in Table S1, the percentages of the H-a, O-b, O-c and O-d shapes are 9%, 10%, 40%, and 41%, respectively. Generally, {200} facets dominate the surface, {220} facets occupy the edges, and {111} facets occupy the vertices of the polyhedron. As listed in Tables S1 and S2, the octagonal shapes (O-b, O-c and O-d) corresponding to the 26-facet polyhedrons account for 91%, and the {200} facets account for 90% of the total surface of the bevelled cube model with octagonal (O-c) shape. The surface area of {200} facets accounts for 58% of the total surface area of 26-facet polyhedrons, based on the statistic TEM images of Rh<sub>2</sub>P-900 NPs. Table S3 summarizes the area proportions of the {200}, {220} and {111} facets on Rh<sub>2</sub>P polyhedrons in Rh<sub>2</sub>P-500, Rh<sub>2</sub>P-600, Rh<sub>2</sub>P-700, Rh<sub>2</sub>P-800, Rh<sub>2</sub>P-900, and Rh<sub>2</sub>P-1000. The area proportion of {200} facets in Rh<sub>2</sub>P-500, Rh<sub>2</sub>P-600, Rh<sub>2</sub>P-700, Rh<sub>2</sub>P-800, Rh<sub>2</sub>P-900, and Rh<sub>2</sub>P-1000 NPs is 26%, 27%, 37%, 35%, 58% and 35%, respectively.

Furthermore, the formation mechanism of the polyhedral Rh<sub>2</sub>P NPs is studied in detail as follows. Fig. 4a shows the thermal gravimetric analysis (TGA) plot of the precursor [Rh(PPh<sub>3</sub>)<sub>3</sub>Cl] in Ar atmosphere. The decomposition of Rh(PPh<sub>3</sub>)<sub>3</sub>Cl starts at about 230 °C and the TGA plot tends to be flat at about 500 °C, 67% of the weight is lost, according to the equation Rh(PPh<sub>3</sub>)<sub>3</sub>Cl → PPh<sub>3</sub> + Rh<sub>2</sub>P + 2HCl(g). Initially, Rh(PPh<sub>3</sub>)<sub>3</sub>Cl is decomposed into RhCl and triphenylphosphine (PPh<sub>3</sub>), then PPh<sub>3</sub> is decomposed into phosphine (PH<sub>3</sub>) gas at 230 °C or higher. Simultaneously, the monovalent Rh of Rh(PPh<sub>3</sub>)<sub>3</sub>Cl is reduced into metallic Rh under the PH<sub>3</sub> atmosphere, resulting in the nucleation and growth of Rh. As the concentration of PH<sub>3</sub> is increased gradually, on one hand, the adsorption of PH<sub>3</sub> on Rh might suppress the rapid growth of Rh, on the other hand, the incorporation of P species could promote the reaction with Rh into Rh<sub>2</sub>P. Essentially, the nucleation and growth of Rh<sub>2</sub>P follow the classical nucleation theory [39,40]. Fig. 4b schematically shows the morphological evolution of Rh<sub>2</sub>P particles. As shown in the TGA plot (Fig. 4a), the curve becomes flatter at about 500 °C, indicating the formation of Rh<sub>2</sub>P nanoparticles, which is consistent with the XRD pattern of Rh<sub>2</sub>P-500 (Fig. S1). However, the Rh<sub>2</sub>P-500 nanoparticles present irregular and spheroidal shapes, as observed from the HR-TEM images (Fig. S4). This can be ascribed to the undifferentiated growth of all the crystal planes as a result of the high reactant concentration of PH<sub>3</sub>. When the reaction temperature is elevated up to 900 °C, the volatilization of the reactants becomes remarkable. So, the lower reactants concentration trigger the different growth rate of various planes, resulting in the formation of 26-facets Rh<sub>2</sub>P polyhedron (Fig. S8). With the reaction temperature is elevated up to 1000 °C, the

morphology of Rh<sub>2</sub>P nanoparticles becomes irregular once again (Fig. S9), it may be attributed to the fast mass transportation that occurs at the higher temperature, leading to the rapidly coalesce of smaller Rh<sub>2</sub>P particles and grow into larger ones with disordered surfaces.

### 3.2. Compositions and chemical states of Rh/C, Rh/Rh<sub>2</sub>P, and Rh<sub>2</sub>P catalysts

The surface chemical states of Rh/C, Rh/Rh<sub>2</sub>P, and Rh<sub>2</sub>P-900 are analyzed by X-ray photoelectron spectroscopy (XPS). All the binding energies are calibrated by the C 1 s at 284.8 eV [41]. Fig. S16 shows the survey spectra and C 1 s spectra of Rh/C, Rh/Rh<sub>2</sub>P, and Rh<sub>2</sub>P-900 [41, 42]. As shown in Fig. 5a, the Rh 3d spectrum can be fitted into four peaks, corresponding to metallic Rh and oxidized Rh. The peaks at 307.6 and 312.3 eV are assigned to 3d<sub>5/2</sub> and 3d<sub>3/2</sub> orbitals of Rh [43–45]. The binding energy of Rh in Rh<sub>2</sub>P is positively shifted, owing to the charge transfer from Rh to P. The peaks at 308.6 and 313.6 eV are ascribed to 3d<sub>5/2</sub> and 3d<sub>3/2</sub> orbitals of oxidized Rh [43]. As shown in Fig. 5b, the peaks at 130.0 and 130.9 eV are assigned to 2p<sub>3/2</sub> and 2p<sub>1/2</sub> orbitals of P in Rh<sub>2</sub>P [41–45]. The binding energy of P 2p<sub>3/2</sub> is lower than that of zero valence P, confirming the charge transfer from Rh to P. The broadened peak at 133.6 eV can be ascribed to the oxidation of the dissociative P adsorbed on the metallic Rh [43–45].

X-ray absorption near-edge spectroscopy (XANES) and the extended X-ray absorption fine structure (EXAFS) spectra are measured to survey the local coordination information of Rh in the Rh/Rh<sub>2</sub>P and Rh<sub>2</sub>P catalysts. The spectra were calibrated with Rh foil and Rh<sub>2</sub>O<sub>3</sub>. The fitted bond lengths, coordination numbers, and other coordination information are listed in Table S4. Fig. 5c shows the K-edge XANES spectra of Rh in Rh/Rh<sub>2</sub>P, Rh<sub>2</sub>P, Rh(I) and Rh(II) references. As compared with the Rh(I), the upshift of the XANES edge suggests the strengthened oxidation state of Rh in Rh<sub>2</sub>P NPs (Fig. 5c, inset). The absorption edge of Rh<sub>2</sub>P NPs is between those of Rh(I) and Rh(II), indicating the middle valence states [32]. Fig. 5d, e plot the wavelet transform contour of Rh/Rh<sub>2</sub>P and Rh<sub>2</sub>P for the  $k^3$ -weighted  $\chi(k)$  signals. The peaks A and B are respectively assignable to Rh–P and Rh–Rh bonds in Rh/Rh<sub>2</sub>P and Rh<sub>2</sub>P [46]. Fourier transform method is adopted to convert the K-edge EXAFS spectra of Rh to R space, and the results are shown in Fig. 5f. As listed in Table S3, the length of Rh–Rh and Rh–P bonds in Rh<sub>2</sub>P NPs is fitted to be 2.73 Å and 2.28 Å, respectively, which is consistent of the perfect crystal structure of Rh<sub>2</sub>P [46].

### 3.3. HER catalytic properties

The electrocatalytic HER activities of Rh/C, Rh/Rh<sub>2</sub>P, Rh<sub>2</sub>P-900, and Pt/C are evaluated in both acidic (0.5 M H<sub>2</sub>SO<sub>4</sub>) and alkaline (1.0 M KOH) electrolytes with a standard three-electrode system. The commercial Pt/C (20 wt%) is used as the benchmark, and all the potential

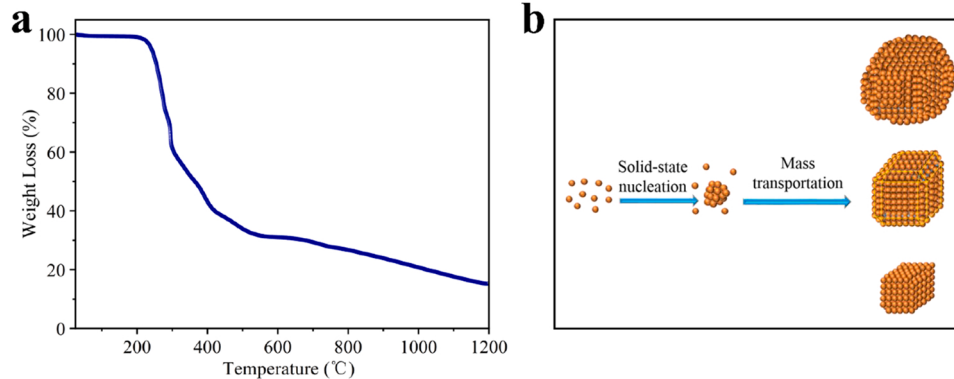


**Fig. 4.** The growth schematic of Rh<sub>2</sub>P nanoparticle. (a) The thermal gravimetric plot of the precursor [Rh(PPh<sub>3</sub>)<sub>3</sub>Cl] in Ar atmosphere. (b) The shape evolution for Rh<sub>2</sub>P nanoparticles.

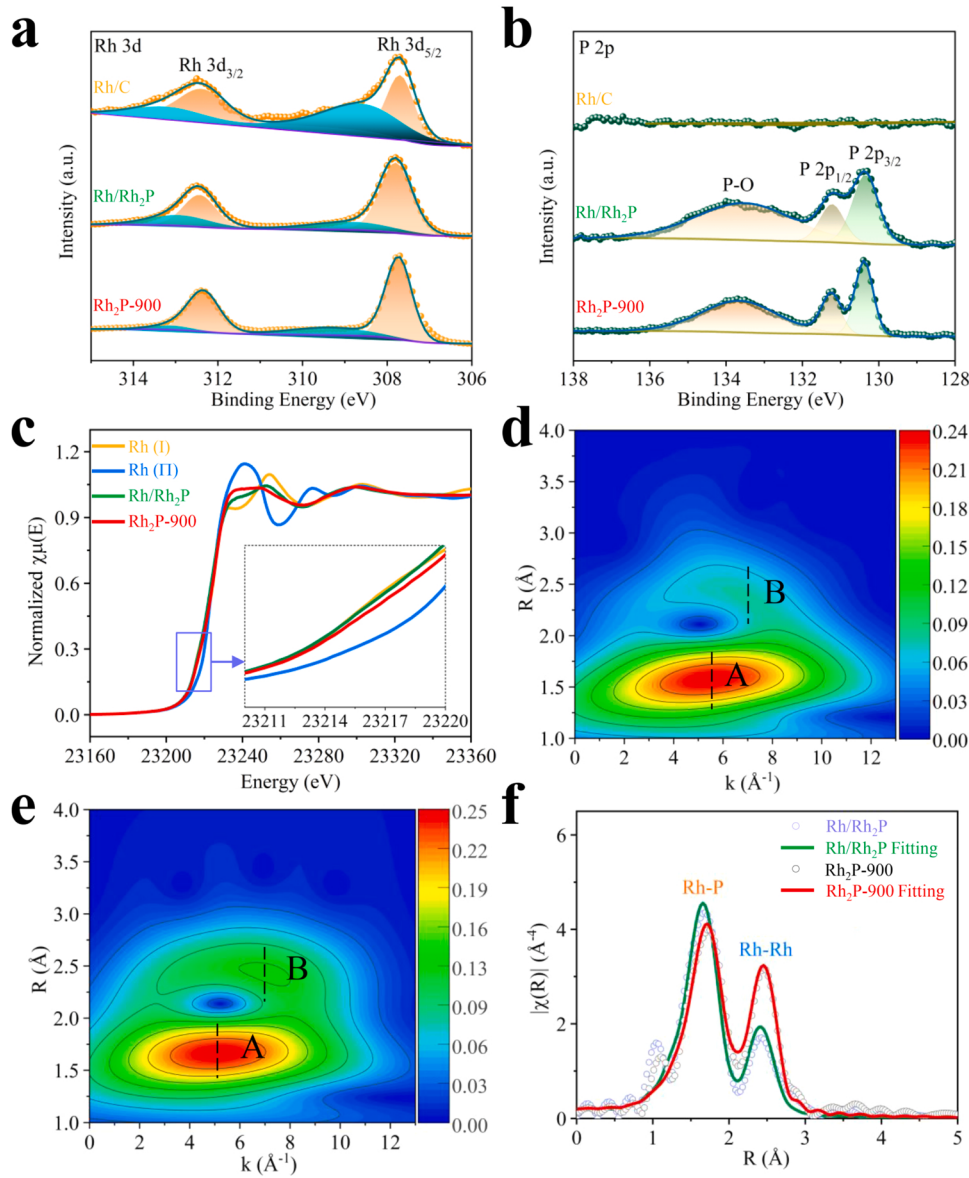


**Fig. 5.** XPS spectra and X-ray absorption fine structure spectra of different catalysts. (a) The Rh 3d and (b) P 2p spectra for Rh/C, Rh/Rh<sub>2</sub>P, and Rh<sub>2</sub>P-900. (c) The Rh K-edge XANES spectra of Rh/Rh<sub>2</sub>P, Rh<sub>2</sub>P-900 catalysts, Rh (I) and Rh (II) references. The wavelet transform of the Rh K-edge EXAFS spectra of (d) Rh/Rh<sub>2</sub>P and (e) Rh<sub>2</sub>P-900, the intensity maximum A is assignable to the Rh–P path, while B is associated with the Rh–Rh path. (f) The Fourier transformed Rh K-edge EXAFS spectra of Rh/Rh<sub>2</sub>P and Rh<sub>2</sub>P-900 catalysts.

data are calibrated with the reversible hydrogen electrode without *iR* compensation. Fig. 6a shows the geometric linear sweep voltammetry (LSV) curves of Rh/C, Rh/Rh<sub>2</sub>P, Rh<sub>2</sub>P-900, and Pt/C in N<sub>2</sub>-saturated 0.5 M H<sub>2</sub>SO<sub>4</sub> at room temperature with the same scan rate of 5 mV s<sup>-1</sup>. Rh/C and Rh/Rh<sub>2</sub>P exhibit the overpotentials of 54.7 mV and 28.6 mV (Figs. 6a and 6i), respectively, which are higher than that of Pt/C (26.8 mV) at the geometric current density of 10 mA cm<sup>-2</sup> ( $\eta_{10}$ ). Rh<sub>2</sub>P-900 exhibits superior HER catalytic activity with the lowest overpotential of 12.6 mV. The Tafel slopes of Rh/C, Rh/Rh<sub>2</sub>P, Rh<sub>2</sub>P-900, and Pt/C are 54.4, 44.0, 35.7, and 41.2 mV dec<sup>-1</sup>, respectively (Fig. 6b). Among them, Rh<sub>2</sub>P-900 displays the fastest HER reaction kinetics and undergoes the Volmer–Heyrovsky mechanism [47]. Cyclic voltammetry (CV) sweeps and chronopotentiometry tests are performed to assess the long-term stability of Rh<sub>2</sub>P-900. As shown in Fig. 6c, the LSV curves of Rh<sub>2</sub>P-900 before and after 2000 CV cycles at a scan rate of 120 mV s<sup>-1</sup> almost coincide with no shift of  $\eta_{10}$ , showing excellent stability. In addition, the chronopotentiometry test of Rh<sub>2</sub>P-900 is carried out at 15 mV vs RHE for 35 h, and only a slight degradation is evidenced after the test (Fig. 6c, inset). The results confirm the outstanding long-term durability of Rh<sub>2</sub>P-900. Furthermore, the morphology of Rh<sub>2</sub>P-900 is almost unchanged after the HER durability test (Fig. S17).

The HER activities of Rh/C, Rh/Rh<sub>2</sub>P, Rh<sub>2</sub>P-900 and Pt/C in the N<sub>2</sub>-saturated alkaline medium are also evaluated (Fig. 6d–f). Compared with the overpotentials of Rh/C (94.5 mV), Rh/Rh<sub>2</sub>P (31.6 mV), and Pt/C (40.2 mV) at  $\eta_{10}$ , Rh<sub>2</sub>P-900 has the lowest overpotential of 10.5 mV (Figs. 6d and 6i). Tafel slopes of Rh/C, Rh/Rh<sub>2</sub>P, Rh<sub>2</sub>P-900 and Pt/C are 133.8, 69.1, 42.7 and 73.4 mV dec<sup>-1</sup>, respectively (Fig. 6e). After 2000 cycles of CV measurements, the polarization curves are only degenerated by 5 mV at  $\eta_{10}$  (Fig. 6f). Long-term durability tests of Rh<sub>2</sub>P-900 at 13 mV vs RHE displays 10% loss of current density after tested for 35 h (inset of Fig. 6f). The uniform particle distribution and morphology features are maintained after durability measurements (Fig. S18). It indicates that Rh<sub>2</sub>P-900 also exhibits excellent durability in alkaline electrolytes. The electrochemical impedance spectroscopy (EIS) and double layered capacitances ( $C_{dl}$ ) are adopted to estimate the charge transfer kinetics and the electrochemically active surface areas in acid medium. Nyquist plots in Fig. 6g reveal that Rh<sub>2</sub>P-900 has the smallest charge transfer resistance ( $R_{ct}$ ). As shown in Fig. 6h, the  $C_{dl}$  values of Rh/C, Rh/Rh<sub>2</sub>P, Rh<sub>2</sub>P-900, and Pt/C are 8.2, 5.4, 17.0, and 13.3 mF m<sup>-2</sup>, respectively. The largest electrochemically active surface area (ECSA) of Rh<sub>2</sub>P-900 confirms the substantially enhanced catalytic activity even better than the benchmark Pt/C (Fig. S19). The other

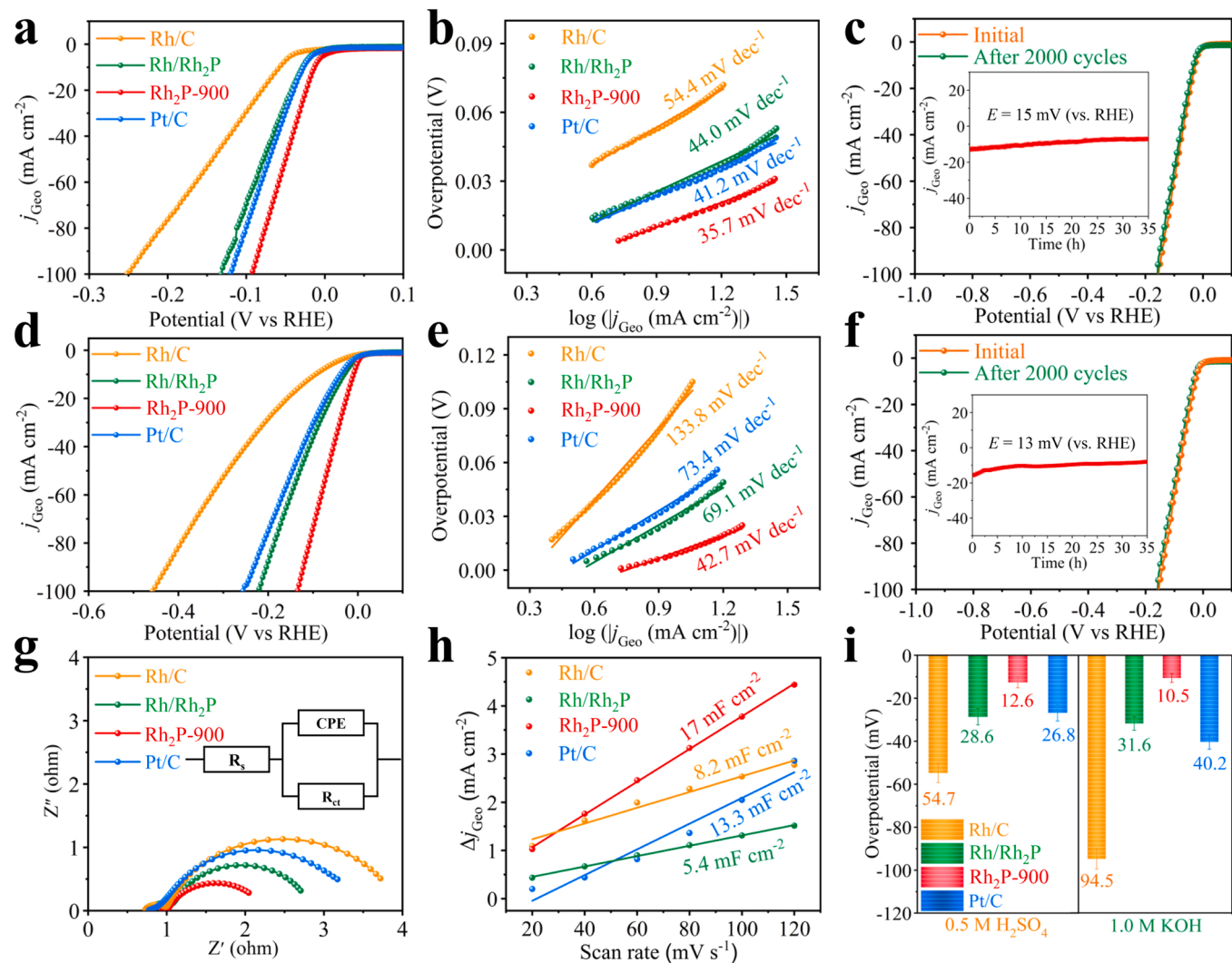


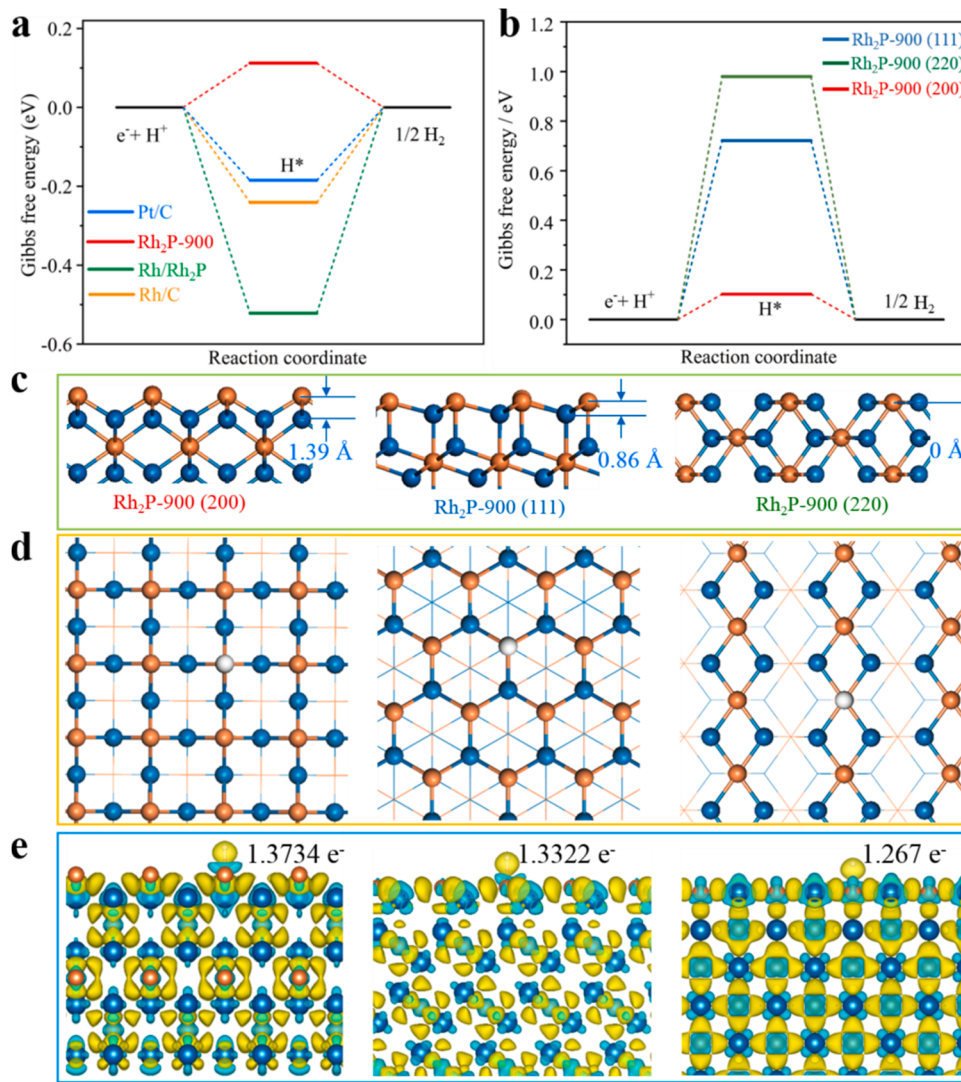
**Fig. 6.** HER catalytic properties of Rh/C, Rh/Rh<sub>2</sub>P, Rh<sub>2</sub>P-900, and Pt/C samples. (a) Geometric linear sweep voltammetry (LSV) curves in 0.5 M H<sub>2</sub>SO<sub>4</sub>. (b) Tafel plots in 0.5 M H<sub>2</sub>SO<sub>4</sub>. (c) Polarization curves of Rh<sub>2</sub>P-900 before and after 2000 CV cycles in 0.5 M H<sub>2</sub>SO<sub>4</sub>, inset is the  $i - t$  curve at 15 mV (vs. RHE). (d) LSV curves in 1.0 M KOH. (e) Corresponding Tafel plots. (f) Polarization curves of Rh<sub>2</sub>P-900 before and after 2000 CV cycles in 1.0 M KOH, inset is the  $i - t$  curve at 13 mV (vs. RHE). (g) The Nyquist plots in 0.5 M H<sub>2</sub>SO<sub>4</sub> under -0.01 V (vs. RHE) in the frequency range from 100 kHz to 1 Hz. (h) Capacitive current in 0.5 M H<sub>2</sub>SO<sub>4</sub> at different scan rates. (i) Overpotential Histograms of different catalysts at 10 mA cm<sup>-2</sup> in 0.5 M H<sub>2</sub>SO<sub>4</sub> (left) and 1.0 M KOH (right).

electrochemical results in alkaline electrolytes are shown in Fig. S20, S21 and S22. Among Rh/C, Rh/Rh<sub>2</sub>P, Rh<sub>2</sub>P-900 and Pt/C, Rh<sub>2</sub>P-900 shows the highest mass activities at 0.05 V (vs RHE) for HER in both acidic and alkaline electrolyte (Fig. S23). It is worth noting that the HER performances of Rh<sub>2</sub>P-900 with polyhedral nanoparticles are substantially higher than those of Rh<sub>2</sub>P-500, Rh<sub>2</sub>P-600, Rh<sub>2</sub>P-700, Rh<sub>2</sub>P-800, Rh<sub>2</sub>P-1000 with irregular morphologies (Fig. S24, S25). Fig. S26 shows the relationship between HER activity ( $\eta_{10}$  and Tafel plots) and the area proportion of {200} facets in the series of Rh<sub>2</sub>P samples under 0.5 M H<sub>2</sub>SO<sub>4</sub> and 1.0 M KOH. Evidently, the HER performances are positively related with the area proportion of the {200} facets in polyhedral Rh<sub>2</sub>P NPs. The dominant {200} facets (58%) in Rh<sub>2</sub>P-900 NPs provide the high catalytic activity, and thus Rh<sub>2</sub>P-900 NPs exhibit the best HER performances. Table S5 summarizes the Tafel slopes and overpotentials at 10 mA cm<sup>-2</sup> of the recently reported HER catalysts, apparently, the polyhedral Rh<sub>2</sub>P-900 NPs also exhibits the best catalytic performances (Fig. S27, S28).

### 3.4. Density functional theory (DFT) calculations

DFT calculations are carried out to obtain deep insight into the

outstanding HER activities of polyhedral Rh<sub>2</sub>P. The detailed DFT calculations are described in the experimental section. The Gibbs free energy of hydrogen adsorption ( $\Delta G_{\text{H}^*}$ ) on the catalyst is calculated to estimate the HER catalytic activities [48]. Fig. 7a shows the  $\Delta G_{\text{H}^*}$  of Rh/C, Rh/Rh<sub>2</sub>P, Rh<sub>2</sub>P-900 and Pt/C. The Gibbs free energy of proton adsorption on Rh<sub>2</sub>P-900 is closer to zero, with respect to that of Rh/C, Rh/Rh<sub>2</sub>P and Pt/C, owing to the transfer of electrons from Rh to P, supported by XPS results in Fig. 5a, b. As mentioned above, {200}, {111}, and {220} planes are the dominant facets in the polyhedral Rh<sub>2</sub>P-900 NPs. Figs. 7c and 7d illustrate the atomic models of the {200}, {111}, and {220} planes of Rh<sub>2</sub>P. The vertical distances between the surface P atoms and the subsurface Rh atoms on {200} and {111} facets in Rh<sub>2</sub>P-900 are 1.39 Å and 0.86 Å, respectively. However, P and Rh atoms are on the same atomic layer of {220} facets. The position and spatial distance of atoms on the different planes of Rh<sub>2</sub>P might affect the catalytic activity substantially. Consequently, the  $\Delta G_{\text{H}^*}$  values of {200}, {111}, and {220} planes of Rh<sub>2</sub>P are also calculated for comparison. The results show that the  $\Delta G_{\text{H}^*}$  value is ranked in the order of {220} > {111} > {200}, suggesting the best HER activity of {200} facets (Fig. 7b). Fig. S29 shows the models of the adsorption and activation of H<sub>2</sub>O and the adsorption of H<sup>\*</sup> species on the P-terminal of Rh<sub>2</sub>P (200), Rh<sub>2</sub>P



(220), and Rh<sub>2</sub>P (111). Fig. S30 displays the transition state energy barrier of water dissociation on the P-terminal of Rh<sub>2</sub>P (200), Rh<sub>2</sub>P (220), and Rh<sub>2</sub>P (111), it is 0.660, 0.904 and 1.107 eV, respectively. The H<sub>2</sub>O molecules absorbed on the P sites of Rh<sub>2</sub>P (200) are more preferable to be dissociated, as compared with that on Rh<sub>2</sub>P (220) and Rh<sub>2</sub>P (111). Moreover, Heyrovsky step is indeed the rate limiting process of HER in alkaline media, Fig. S31 and Fig. S32 schematically show the energy of transition states in Heyrovsky reaction on P-terminal of Rh<sub>2</sub>P (200), Rh<sub>2</sub>P (220) and Rh<sub>2</sub>P (111). The lower energy (2.497 eV) of (200) plane facilitates water dissociation and accelerates the reaction kinetics of HER under alkaline condition. Fig. S33 shows the partial density of states (PDOS) of the (200), (220), and (111) facets of Rh<sub>2</sub>P. The hybridization between Rh-4d band and P-3p band of Rh<sub>2</sub>P (111) facet is more remarkable than that of Rh<sub>2</sub>P (200) facet. Since the binding strength of H<sup>\*</sup> on Rh<sub>2</sub>P is related to the d-band center with respect to the Fermi level (E<sub>f</sub>) (Table S6), and the d-band center of Rh<sub>2</sub>P (200) facet is more far away from E<sub>f</sub>, the adsorption of H<sup>\*</sup> on P terminal Rh<sub>2</sub>P (200) facet is weaker, leading to a favorable recombination of hydrogen adsorbates. Therefore, Rh<sub>2</sub>P (200) facets exhibit considerable HER activity in both alkaline and acid medium, as illustrated in experiments.

Furthermore, Bede charge analysis is performed to evaluate the electron transfer from the active site to H on the {200}, {111} and {220} planes of Rh<sub>2</sub>P, the results are shown in Fig. 7e. The blue and yellow indicate the charge dissipation and accumulation, respectively. The

**Fig. 7.** Structural models and theoretical calculations. (a) Calculated  $\Delta G_{H\text{-ad}}$  for Rh/C, Rh/Rh<sub>2</sub>P and Rh<sub>2</sub>P-900 and Pt/C. (b) Calculated  $\Delta G_{H\text{-ad}}$  for the Rh<sub>2</sub>P-900 (200), Rh<sub>2</sub>P-900 (111) and Rh<sub>2</sub>P-900 (220) planes. (c, d) The side and top structural models of Rh<sub>2</sub>P-900 (200), Rh<sub>2</sub>P-900 (111) and Rh<sub>2</sub>P-900 (220), dark cyan, orange, and white balls represent rhodium, phosphorus, and hydrogen atoms, respectively. (e) Bader analysis of charge distribution for the Rh<sub>2</sub>P-900 (200), Rh<sub>2</sub>P-900 (111), and Rh<sub>2</sub>P-900 (220) planes. The blue and yellow areas signify the diminution and escalation of the charge, respectively. The isosurfaces were set to 0.007 e  $\text{\AA}^{-3}$ .

degree of overall charge transfer is in the order of {200} > {111} > {220}, by 1.3734, 1.3322 and 1.2670 e<sup>-</sup>, respectively. Therefore, the top P sites in {200} planes of Rh<sub>2</sub>P-900 capture the protons remarkably, resulting in the high catalytic activity of Rh<sub>2</sub>P-900. In brief, the controllable synthesis of polyhedral nanoparticles with high-activity facets is fundamentally important to the exploitation of high-performance HER catalysis.

#### 4. Conclusion

A one-step facile solid-state reaction is proposed to synthesize polyhedral Rh<sub>2</sub>P nanoparticles. The polyhedral Rh<sub>2</sub>P NPs are mainly enclosed by the {200}, {220} and {111} facets. Statistics data demonstrate that the 26-facet polyhedron shapes are dominant, and {200} facets account for 58% of the total facets of 26-facet polyhedron. The polyhedral Rh<sub>2</sub>P nanoparticles exhibit a very low overpotential of 12.6 and 10.5 mV at 10 mA cm<sup>-2</sup> in 0.5 M H<sub>2</sub>SO<sub>4</sub> and 1.0 M KOH solutions, respectively, which even exceeds the state-of-the-art commercial Pt/C catalysts. Theoretical calculations suggest that the enhanced catalytic activity is ascribed to the optimum hydrogen adsorption Gibbs free energy of {200} facets, compared with those of {220} and {111} facets. The results will further support the design of the polyhedron shape with the rich active crystal plane toward the HER and other energy conversion reactions.

## CRediT authorship contribution statement

**Hongqiang Xin:** Validation, Formal analysis, Investigation, Data curation, Visualization, Writing – original draft. **Lan Sun:** Software. **Yiwei Zhao:** Software. **Zhengfei Dai:** Supervision, Writing – review & editing. **Qiaomei Luo:** Formal analysis, Writing – review & editing. **Shengwu Guo:** Methodology, Writing – review & editing. **Danyang Li:** Formal analysis, Methodology. **Ya Chen:** Methodology. **Naoki Ogawa:** Resources. **Hiroshi Kitagawa:** Resources. **Bo Huang:** Supervision, Funding acquisition, Writing – review & editing. **Fei Ma:** Supervision, Funding acquisition, Writing – review & editing.

## Declaration of Competing Interest

The authors declare that they have no known competing financial interests or personal relationships that could have appeared to influence the work reported in this paper.

## Data availability

Data will be made available on request.

## Acknowledgments

This work was jointly supported by the National Natural Science Foundation of China (Nos. 52271136, 22001202), Natural Science Foundation of Shaanxi Province (Nos. 2019TD-020, 2021JC-06). This research used the resources of the HPCC platform in Xi'an Jiaotong University. We thank Chenyu Liang at the Instrument Analysis Center of Xi'an Jiaotong University for his assistance with XPS analysis. We acknowledge Research Fellow Yanhuai Li and Wei Wang of Xi'an Jiaotong University for the help of TEM and SEM characterization. We are thankful to Dr. T. Honma of JASRI for technical support during the collection of XAFS. The XAFS measurements were performed with the approval of JASRI (Proposal No. 2018B1728).

## Appendix A. Supporting information

Supplementary data associated with this article can be found in the online version at [doi:10.1016/j.apcatb.2023.122645](https://doi.org/10.1016/j.apcatb.2023.122645).

## References

- [1] Z.W. Seh, J. Kibsgaard, C.F. Dickens, I. Chorkendorff, J.K. Norskov, T.F. Jaramillo, Combining theory and experiment in electrocatalysis: Insights into materials design, *Science* 355 (2017) eaad4998, <https://doi.org/10.1126/science.aad4998>.
- [2] T. Kosmala, A. Baby, M. Lunardon, D. Perilli, H. Liu, C. Durante, C. Di Valentini, S. Agnoli, G. Granozzi, Operando visualization of the hydrogen evolution reaction with atomic-scale precision at different metal–graphene interfaces, *Nat. Catal.* 4 (2021) 850–859, <https://doi.org/10.1038/s41929-021-00682-2>.
- [3] Z. Sun, W. Shi, C. Pei, C.K. Russell, D. Cheng, Z. Sun, J. Gong, Tailoring lattice oxygen triggered NiO/Ca<sub>9</sub>Co<sub>12</sub>O<sub>28</sub> catalysts for sorption-enhanced renewable hydrogen production, *Appl. Catal. B* 316 (2022), <https://doi.org/10.1016/j.apcatb.2022.121642>.
- [4] M. Blasco-Ahicart, J. Soriano-Lopez, J.J. Carbo, J.M. Poblet, J.R. Galan-Mascaros, Polyoxometalate electrocatalysts based on earth-abundant metals for efficient water oxidation in acidic media, *Nat. Chem.* 10 (2018) 24–30, <https://doi.org/10.1038/nchem.2874>.
- [5] N. Bekirsky, C.E. Hoicka, M.C. Brisbois, L. Ramirez Camargo, Many actors amongst multiple renewables: a systematic review of actor involvement in complementarity of renewable energy sources, *Renew. Sustain. Energ. Rev.* 161 (2022), 112368, <https://doi.org/10.1016/j.rser.2022.112368>.
- [6] T. Zhang, Y. Liu, J. Yu, Q. Ye, L. Yang, Y. Li, H.J. Fan, Biaxially strained MoS<sub>2</sub> nanoshells with controllable layers boost alkaline hydrogen evolution, *Adv. Mater.* 34 (2022), e2202195, <https://doi.org/10.1002/adma.202202195>.
- [7] T. Wang, L. Tao, X. Zhu, C. Chen, W. Chen, S. Du, Y. Zhou, B. Zhou, D. Wang, C. Xie, P. Long, W. Li, Y. Wang, R. Chen, Y. Zou, X.-Z. Fu, Y. Li, X. Duan, S. Wang, Combined anodic and cathodic hydrogen production from aldehyde oxidation and hydrogen evolution reaction, *Nat. Catal.* 5 (2021) 66–73, <https://doi.org/10.1038/s41929-021-00721-y>.
- [8] J. Lee, C. Yeon, J. Oh, G. Han, J. Do Yoo, H.J. Yun, C.-W. Lee, K.T. Lee, J. Bae, Highly active and stable catalyst with exsolved PtRu alloy nanoparticles for hydrogen production via commercial diesel reforming, *Appl. Catal. B* 316 (2022), <https://doi.org/10.1016/j.apcatb.2022.121645>.
- [9] Y. Li, Y. Sun, Y. Qin, W. Zhang, L. Wang, M. Luo, H. Yang, S. Guo, Recent advances on water-splitting electrocatalysis mediated by noble-metal-based nanostructured materials, *Adv. Energy Mater.* 10 (2020), 1903120, <https://doi.org/10.1002/aenm.201903120>.
- [10] M. Chatenet, B.G. Pollet, D.R. Dekel, F. Dionigi, J. Deseure, P. Millet, R.D. Braatz, M.Z. Bazant, M. Eikerling, I. Staffell, P. Balcombe, Y. Shao-Horn, H. Schafer, Water electrolysis: from textbook knowledge to the latest scientific strategies and industrial developments, *Chem. Soc. Rev.* 51 (2022) 4583–4762, <https://doi.org/10.1039/d0cs01079k>.
- [11] J. Li, S. Wang, J. Chang, L. Feng, A review of Ni based powder catalyst for urea oxidation in assisting water splitting reaction, *Adv. Powder Mater.* 1 (2022), 100030, <https://doi.org/10.1016/j.apmate.2022.01.003>.
- [12] Q. Zhou, Q. Hao, Y. Li, J. Yu, C. Xu, H. Liu, S. Yan, Free-standing trimodal porous NiZn intermetallic and Ni heterojunction as highly efficient hydrogen evolution electrocatalyst in the alkaline electrolyte, *Nano Energy* 89 (2021), <https://doi.org/10.1016/j.nanoen.2021.106402>.
- [13] Y. Sun, Z. Xue, Q. Liu, Y. Jia, Y. Li, K. Liu, Y. Lin, M. Liu, G. Li, C.Y. Su, Modulating electronic structure of metal-organic frameworks by introducing atomically dispersed Ru for efficient hydrogen evolution, *Nat. Commun.* 12 (2021) 1369, <https://doi.org/10.1038/s41467-021-21595-5>.
- [14] Y. Liu, Y. Chen, Y. Tian, T. Sakthivel, H. Liu, S. Guo, H. Zeng, Z. Dai, Synergizing hydrogen spillover and deprotonation by the internal polarization field in a MoS<sub>2</sub>/NiPS<sub>3</sub> vertical heterostructure for boosted water electrolysis, *Adv. Mater.* (2022), e2203615, <https://doi.org/10.1002/adma.202203615>.
- [15] H. Jing, P. Zhu, X. Zheng, Z. Zhang, D. Wang, Y. Li, Theory-oriented screening and discovery of advanced energy transformation materials in electrocatalysis, *Adv. Powder Mater.* 1 (2022), 100013, <https://doi.org/10.1016/j.apmate.2021.10.004>.
- [16] S.I. Mutinda, T.N. Batugedara, B. Brown, O. Adeniran, Z.-F. Liu, S.L. Brock, Rh<sub>2</sub>P activity at a fraction of the cost? Co<sub>2-x</sub>Rh<sub>x</sub>P nanoparticles as electrocatalysts for the hydrogen evolution reaction in acidic media, *ACS Appl. Energy Mater.* 4 (2021) 946–955, <https://doi.org/10.1021/acsaem.0c02880>.
- [17] S. Yang, X. Yang, Q. Wang, X. Cui, H. Zou, X. Tong, N. Yang, Facet-selective hydrogen evolution on Rh<sub>2</sub>P electrocatalysts in pH-universal media a, *Chem. Eng. J.* 449 (2022), 137790, <https://doi.org/10.1016/j.cej.2022.137790>.
- [18] X. Guo, X. Chen, Y. Huang, X. Min, C. Kong, Y. Tang, B. Liu, Atomically ordered Rh<sub>2</sub>P catalysts anchored within hollow mesoporous carbon for efficient hydrogen production.
- [19] L. Sun, Q. Luo, Z. Dai, F. Ma, Material libraries for electrocatalytic overall water splitting, *Coord. Chem. Rev.* 444 (2021), 214049, <https://doi.org/10.1016/j.ccr.2021.214049>.
- [20] D. Tian, S.R. Denny, K. Li, H. Wang, S. Kattel, J.G. Chen, Density functional theory studies of transition metal carbides and nitrides as electrocatalysts, *Chem. Soc. Rev.* 50 (2021) 12338–12376, <https://doi.org/10.1039/d0cs00590a>.
- [21] M. Zubair, M.M. Ul Hassan, M.T. Mehran, M.M. Baig, S. Hussain, F. Shahzad, 2D MXenes and their heterostructures for HER, OER and overall water splitting: a review, *Int. J. Hydrol. Energy* 47 (2022) 2794–2818, <https://doi.org/10.1016/j.ijhydene.2021.10.248>.
- [22] B. Zhou, R. Gao, J.J. Zou, H. Yang, Surface design strategy of catalysts for water electrolysis, *Small* 18 (2022), 2202336, <https://doi.org/10.1002/smll.202202336>.
- [23] M. Liu, J.A. Wang, W. Klysubun, G.G. Wang, S. Sattayaporn, F. Li, Y.W. Cai, F. Zhang, J. Yu, Y. Yang, Interfacial electronic structure engineering on molybdenum sulfide for robust dual-pH hydrogen evolution, *Nat. Commun.* 12 (2021) 5260, <https://doi.org/10.1038/s41467-021-25647-8>.
- [24] M.T. Chen, R.L. Zhang, J.J. Feng, L.P. Mei, Y. Jiao, L. Zhang, A.J. Wang, A facile one-pot room-temperature growth of self-supported ultrathin rhodium-iridium nanosheets as high-efficiency electrocatalysts for hydrogen evolution reaction, *J. Colloid Interface Sci.* 606 (2022) 1707–1714, <https://doi.org/10.1016/j.jcis.2021.08.144>.
- [25] F. Yang, Y. Zhao, Y. Du, Y. Chen, G. Cheng, S. Chen, W. Luo, A monodisperse Rh<sub>2</sub>P-based electrocatalyst for highly efficient and pH-universal hydrogen evolution reaction, *Adv. Energy Mater.* (2018), 1703489, <https://doi.org/10.1002/aenm.201703489>.
- [26] Y. Zhao, N. Jia, X.-R. Wu, F.-M. Li, P. Chen, P.-J. Jin, S. Yin, Y. Chen, Rhodium phosphide ultrathin nanosheets for hydrazine oxidation boosted electrochemical water splitting, *Appl. Catal. B* 270 (2020), 118880, <https://doi.org/10.1016/j.apcatb.2020.118880>.
- [27] H. Duan, D. Li, Y. Tang, Y. He, S. Ji, R. Wang, H. Lv, P.P. Lopes, A.P. Paulikas, H. Li, S.X. Mao, C. Wang, N.M. Markovic, J. Li, V.R. Stamenkovic, Y. Li, High-performance Rh<sub>2</sub>P electrocatalyst for efficient water splitting, *J. Am. Chem. Soc.* 139 (2017) 5494–5502, <https://doi.org/10.1021/jacs.7b01376>.
- [28] Z. Han, R.-L. Zhang, J.-J. Duan, A.-J. Wang, Q.-L. Zhang, H. Huang, J.-J. Feng, Platinum-rhodium alloyed dendritic nanoassemblies: an all-pH efficient and stable electrocatalyst for hydrogen evolution reaction, *Int. J. Hydrol. Energy* 45 (2020) 6110–6119, <https://doi.org/10.1016/j.ijhydene.2019.12.155>.
- [29] Y.-Q. Yao, Z.-J. Wang, R.-L. Zhang, L. Zhang, J.-J. Feng, A.-J. Wang, Effective construction of 3D Rh/Rh<sub>2</sub>P flake-like assembled heterostructures for efficient hydrogen evolution, *J. Alloy. Compd.* 865 (2021), <https://doi.org/10.1016/j.jallcom.2021.158864>.
- [30] A.E. Henkes, R.E. Schaak, Template-assisted synthesis of shape-controlled Rh<sub>2</sub>P nanocrystals, *Inorg. Chem.* 47 (2008) 671, <https://doi.org/10.1021/ic701783f>.
- [31] N.F. Yu, N. Tian, Z.Y. Zhou, L. Huang, J. Xiao, Y.H. Wen, S.G. Sun, Electrochemical synthesis of tetrahedral rhodium nanocrystals with extraordinarily high surface energy and high electrocatalytic activity, *Angew. Chem. Int. Ed.* 53 (2014) 5097–5101, <https://doi.org/10.1002/anie.201310597>.

- [32] H. Xin, Z. Dai, Y. Zhao, S. Guo, J. Sun, Q. Luo, P. Zhang, L. Sun, N. Ogiwara, H. Kitagawa, B. Huang, F. Ma, Recording the Pt-beyond hydrogen production electrocatalysis by dirhodium phosphide with an overpotential of only 4.3 mV in alkaline electrolyte, *Appl. Catal. B* 297 (2021), 120457, <https://doi.org/10.1016/j.apcatb.2021.120457>.
- [33] G. Kresse, J. Furthmüller, Efficiency of ab-initio total energy calculations for metals and semiconductors using a plane-wave basis set, *Comput. Mater. Sci.* 6 (1996) 15–50, [https://doi.org/10.1016/0927-0256\(96\)00008-0](https://doi.org/10.1016/0927-0256(96)00008-0).
- [34] G. Kresse, J. Furthmüller, Efficient iterative schemes for ab initio total-energy calculations using a plane-wave basis set, *Phys. Rev. B* 54 (1996) 11169–11186, <https://doi.org/10.1103/physrevb.54.11169>.
- [35] John P. Perdew, Kieron Burke, M. Ernzerhof, Generalized gradient approximation made simple, *Phys. Rev. Lett.* 77 (1996) 3865–3868, <https://doi.org/10.1103/PhysRevLett.77.3865>.
- [36] J.K. Nørskov, T. Bligaard, A. Logadottir, J.R. Kitchin, J.G. Chen, S. Pandelov, U. Stimming, Trends in the exchange current for hydrogen evolution, *J. Electrochem. Soc.* 3 (2005) J23–J26, <https://doi.org/10.1149/1.1856988>.
- [37] K. Wang, B. Huang, F. Lin, F. Lv, M. Luo, P. Zhou, Q. Liu, W. Zhang, C. Yang, Y. Tang, Y. Yang, W. Wang, H. Wang, S. Guo, Wrinkled Rh<sub>2</sub>P nanosheets as superior pH-universal electrocatalysts for hydrogen evolution catalysis, *Adv. Energy Mater.* 8 (2018), 1801891, <https://doi.org/10.1002/aenm.201801891>.
- [38] D. Faivre, N. Menguy, M. Posfai, D. Schuler, Environmental parameters affect the physical properties of fast-growing magnetosomes, *Am. Mineral.* 93 (2008) 463–469, <https://doi.org/10.2138/am.2008.2678>.
- [39] N.A. Feoklistov, S.A. Grudinkin, V.G. Golubev, M.A. Baranov, K.V. Bogdanov, S. A. Kukushkin, Evolution of the morphology of diamond particles and mechanism of their growth during the synthesis by chemical vapor deposition, *Phys. Solid State* 57 (2015) 2184–2190, <https://doi.org/10.1134/s1063783415110104>.
- [40] T. Wang, K. Ren, M. He, W. Dong, W. Xiao, H. Pan, J. Yang, Y. Yang, P. Liu, Z. Cao, X. Ma, H. Wang, Synthesis and manipulation of single-crystalline lithium nickel manganese cobalt oxide cathodes: a review of growth mechanism, *Front. Chem.* 8 (2020) 747, <https://doi.org/10.3389/fchem.2020.00747>.
- [41] Q. Qin, H. Jang, L. Chen, G. Nam, X. Liu, J. Cho, Low loading of Rh<sub>x</sub>P and RuP on N, P codoped carbon as two trifunctional electrocatalysts for the oxygen and hydrogen electrode reactions, *Adv. Energy Mater.* 8 (2018), 1801478, <https://doi.org/10.1002/aenm.201801478>.
- [42] R. Wang, X. Wang, M. Cheng, Y. Wei, J. Xia, H. Lin, W. Sun, W. Hu, Phosphatizing engineering of heterostructured Rh<sub>2</sub>P/Rh nanoparticles on doped graphene for efficient hydrogen evolution in alkaline and acidic media, *Int. J. Hydrog. Energy* 47 (2022) 24669–24679, <https://doi.org/10.1016/j.ijhydene.2022.05.212>.
- [43] F. Luo, L. Guo, Y. Xie, J. Xu, W. Cai, K. Qu, Z. Yang, Robust hydrogen evolution reaction activity catalyzed by ultrasmall Rh-Rh<sub>2</sub>P nanoparticles, *J. Mater. Chem. A* 8 (2020) 12378–12384, <https://doi.org/10.1039/dta04773b>.
- [44] Z. Pu, I.S. Amiiu, D. He, M. Wang, G. Li, S. Mu, Activating rhodium phosphide-based catalysts for the pH-universal hydrogen evolution reaction, *Nanoscale* 10 (2018) 12407–12412, <https://doi.org/10.1039/c8nr02854k>.
- [45] S. Pan, X. Yu, Y. Ling, Z. Yang, Stable and efficient hydrogen evolution reaction catalyzed by NiO-Rh<sub>2</sub>P heterostructure electrocatalyst, *Catal. Commun.* 163 (2022), 106404, <https://doi.org/10.1016/j.catcom.2022.106404>.
- [46] C. Galdeano-Ruano, C.W. Lopes, D. Motta Meira, A. Corma, P. Oña-Burgos, Rh<sub>2</sub>P nanoparticles stabilized by carbon patches for hydroformylation of olefins, *ACS Appl. Nano Mater.* 4 (2021) 10743–10753, <https://doi.org/10.1021/acsanm.1c02194>.
- [47] T. Shinagawa, A.T. Garcia-Esparza, K. Takanabe, Insight on Tafel slopes from a microkinetic analysis of aqueous electrocatalysis for energy conversion, *Sci. Rep.* 5 (2015) 13801, <https://doi.org/10.1038/srep13801>.
- [48] B. Hinnemann, P.G. Moses, J. Bonde, K.P. Jørgensen, J.H. Nielsen, S. Horch, I. Chorkendorff, J.K. Nørskov, Biomimetic hydrogen evolution: MoS<sub>2</sub> nanoparticles as catalyst for hydrogen evolution, *J. Am. Chem. Soc.* 127 (2005) 5308–5309, <https://doi.org/10.1021/ja0504690>.